FirePhysChem xxx (xxxx) xxx

Contents lists available at ScienceDirect

FirePhysChem

journal homepage: http://www.keaipublishing.com/cn/journals/firephyschem/

3D-Printed cellular reinforcements: Mechanical and ballistic responses of paraffin-based armored grains

Riccardo Bisin, Francesco Calabró, Christian Paravan*

Department of Aerospace Science and Technology, Politecnico di Milano, 34 via LaMasa, Milan, I-20156, Italy

ARTICLE INFO

Keywords:
Hybrid rocket engine
Paraffin-based fuels
3D-printing
Armored grain
Cellular structures

ABSTRACT

Additive manufacturing enables the fabrication of complex open-cell geometries that can be used as mechanical reinforcements in paraffin-based fuels for hybrid propulsion. In this study, heterogeneous fuel grains are characterized in terms of their mechanical response and burning behavior. Tested formulations feature a 3D-printed reinforcement in polylactic acid, and are named *armored grains*. Four strengthening reinforcements are produced by fused deposition modeling: two triply periodic minimal surface structures (gyroid and Schwarz-P), and two honeycomb-based reinforcements (straight and twisted). Gyroids are contrasted considering different infills (i.e., volume fraction of the 3D-printed part), while different structures are contrasted for a single infill. The results show that all reinforcements markedly increase the yield stress and strain energy of the pristine paraffin, while enhancing the regression rate ($\dot{r}_f$). This result is noteworthy, since reinforcements typically suppress the fast $\dot{r}_f$ of waxes. The uneven surface of the burning grain yields increased heat transfer from the flame to the surface, thus providing faster $\dot{r}_f$. Regression rate enhancement for gyroids and twisted honeycombs is in the range 25%–27% for oxidizer mass flux $\sim 40\ \mathrm{kg/(m^2 \cdot s)}$. Finite-elements analyses on the reinforcing structures capture the observed collapse modes. The performed screening provides structure-property-performance details for the design of 3D-printed reinforcements in paraffin-based fuels for hybrid propulsion. Gyroids emerge as suitable structures for grain reinforcement given their stress distribution and small-scale $\dot{r}_f$ performance.

1. Introduction

Low-cost access to space drives the search for propulsive technologies that are affordable, safe, environmentally friendly, and flexible. Hybrid rocket engines (HREs) can meet these requirements, offering attractive possibilities for both small launch systems and in-space propulsion [1–3]. However, the appealing features of HREs are hindered by the slow solid regression rate ($\dot{r}_f$) of conventional polymeric formulations (e.g., hydroxyl-terminated polybutadiene, HTPB). Reduced $\dot{r}_f$ implies large regressing surface areas to provide high thrust levels, and this limits the use of simple grain geometries and standard oxidizer injection implementations. Liquefying fuels featuring entrainment mass transfer offer a disruptive route toward faster $\dot{r}_f$ [4–6], and are the subject of efforts from different start-ups such as HyImpulse (Germany) [7], Gilmour Space Technologies (Australia) [8], TiSpace (Taiwan) [9], and Innospace (South Korea) [10]. Entrainment of melted fuel droplets is a mass transfer mechanism due to the low viscosity and low surface tension of special liquefying fuels such as paraffin waxes. When entrainment is triggered, $\dot{r}_f$ and fuel mass burning rate are enhanced. On the other hand, a major drawback of paraffin waxes is their weak mechanical behavior (brittle and frail under load [11]). A common reinforcing strategy consists in blending the wax with polymeric additives, which improves the mechanical properties but alters the melt-phase behavior and reduces the $\dot{r}_f$ [12,13]. Current research efforts are therefore devoted to paraffin-based fuels that combine suitable mechanical characteristics with fast $\dot{r}_f$.

The Space Propulsion Laboratory (SPLab) of Politecnico di Milano is developing innovative hybrid rocket fuels combining stronger mechanical properties with fast $\dot{r}_f$. A novel reinforcement approach, termed *armored grain*, has been recently proposed [11,14]. In this concept, a triply periodic minimal surface (TPMS) open-cell structure is embedded within the paraffin grain to enhance its mechanical response while preserving intense entrainment mass transfer of the liquefying fuel, thereby exploiting both the attractive features of paraffin waxes and the design flexibility of additive manufacturing (AM). The present study provides a detailed investigation of armored grains based on a single macro-crystalline paraffin wax reinforced by different 3D-printed structures. Polylactic acid (PLA) is selected as the reinforcement ma-

Peer review under the responsibility of Editorial Board of FirePhysChem.
* Corresponding author.
E-mail addresses: riccardo.bisin@polimi.it (R. Bisin), francesco.calabro@polimi.it (F. Calabró), christian.paravan@polimi.it (C. Paravan).

https://doi.org/10.1016/j.fpc.2026.05.009
Received 31 December 2025; Received in revised form 27 May 2026; Accepted 28 May 2026
Available online xxx

Please cite this article as: R. Bisin, F. Calabró and C. Paravan, 3D-printed cellular reinforcements: Mechanical and ballistic responses of paraffin-based armored grains, FirePhysChem, https://doi.org/10.1016/j.fpc.2026.05.009

Nomenclature

Acronyms and abbreviations

ABS	Acrylonitrile butadiene styrene
CP	Graphite powder
FDM	Fused deposition modeling
FEA	Finite element analysis
HRE	Hybrid rocket engine
HTPB	Hydroxyl-terminated polybutadiene
MB	Mass-based (regression rate data reduction technique)
NY	Nylon 6
PLA	Polylactic acid
SEBS-MA	Styrene-ethylene-butylene-styrene copolymer grafted with maleic anhydride
SPLab	Space propulsion laboratory
TMD	Theoretical maximum density
TPI	Turns per inch
TPMS	Triply periodic minimal surface

Latin and Greek symbols

$\overline{G}_{ox}$	Time- and space-averaged oxidizer mass flux, $kg/(m^2 \cdot s)$
$\overline{p}_c$	Time-averaged combustion chamber pressure, MPa
Δt_b	Burning time, s
$\dot{m}_f$	Fuel mass flow rate, g/s
$\dot{m}_{ox}$	Oxidizer mass flow rate, g/s
$\dot{r}_f$	Solid fuel regression rate, mm/s
ρ	Density, g/cm^3
ρ_f	Solid fuel density, g/cm^3
D	Diameter, mm
d	Printed layer thickness, mm
E	Young modulus, MPa
G_{ox}	Oxidizer mass flux, $kg/(m^2 \cdot s)$
L	Characteristic unit cell size of the cellular structure, mm
m	Mass, g
p_c	Combustion chamber pressure, MPa
t	Time, s
t_{end}	Final time, s
t_{in}	Initial time, s

Other symbols

ϵ	Strain, %
ϵ_y	Strain at yield, %
$\tilde{\rho}_{\%}$	Percent relative density of a cellular structure, %
σ	Stress, MPa
σ_y	Stress at yield, MPa

terial, and fused deposition modeling (FDM) is adopted as the printing process. Four reinforcement architectures are considered: gyroid (GY), Schwarz-P (SP), straight honeycomb (SH), and twisted honeycomb with 1/4 turns per inch (TH). The GY and the SP are TPMS. Gyroids with *infills* (i.e., volume fractions) of 7%, 10%, and 15% are considered. The work proceeds in two main steps: (i) mechanical characterization of the reinforcing structures, and (ii) mechanical and ballistic analyses of the corresponding armored grains. The mechanical properties of the reinforcements are investigated through compression tests and finite element analysis (FEA). The mechanical response and ballistic performance of the armored grains are assessed by compression tests, FEA on simplified geometries, and combustion runs in a lab-scale hybrid rocket engine. The purpose of this study is to clarify the links between reinforcement architecture, mechanical properties, and regression behavior, and to assess the feasibility of 3D-printing as a methodology to produce a new class of green, high-performance paraffin-based fuels.

2. Background on paraffin-based fuels and their reinforcing strategies

In the late 1990s, St. Clair et al. [15] reported the fast $\dot{r}_f$ of cryogenic fuels for hybrid propulsion. Subsequent analyses led to the identification of the conditions under which a fuel that forms a melt layer at the regressing surface can exhibit increased $\dot{r}_f$ [4,5]. This enhanced performance is achieved by the combination of the (conventional) fuel vaporization with a mechanical effect called *entrainment*. Entrainment mass transfer is due to the unstable behavior of the liquid layer formed at the grain surface. Such unstable behavior is achieved under the shear action of the gas stream, when melt viscosity and surface tension are sufficiently low [4,5]. Paraffin waxes are the most common liquefying fuels exhibiting fast $\dot{r}_f$ thanks to the entrainment mass transfer. Despite their attractive ballistic performance, paraffin waxes show a brittle and frail mechanical behavior, with a relatively high Young's modulus (E, in the range 500 MPa to 800 MPa [16,17]) and small strains (ϵ) at failure (typically below a few percent, say 0.5% to 1.3% [18]). Macro- and micro-crystalline waxes mainly differ in terms of chemical composition and thermo-physical properties [16,17]. Macro-crystalline waxes, rich in normal alkanes, feature relatively low melting points (320–345 K) and lower melt viscosities than their micro-crystalline counterparts [19]. This combination of fast $\dot{r}_f$ and weak mechanical behavior motivates the search for suitable reinforcement strategies. A first, widely explored route is blending paraffin waxes with strengthening polymers. A review and critical analysis of thermosetting polymers as reinforcing agents is provided by Thomas et al. [20]. Focusing on the more commonly implemented blending with thermoplastic strengthening polymers, several examples are discussed in the literature: high-density polyethylene (HDPE) [21], ethylene-vinyl acetate (EVA) and styrene-ethylene-butadiene-styrene grafted with maleic anhydride (SEBS-MA) [11,13,22], as well as tackifiers [23]. Overall, polymer blending (i) has limited impacts on the reinforcement of the wax-based fuel mechanical properties [11,18], (ii) does not significantly alter the fuel melting temperature [12,13,23], and (iii) implies an increase in the melt-phase viscosity that, in turn, yields a reduction of the entrainment mass transfer [12,13,19,24]. A trade-off between mechanical and ballistic properties is therefore inherent to formulation-based reinforcement strategies. Additive manufacturing has been introduced as a technique for solid fuel grain production by the pioneering works of Whitmore and co-workers [25–27]. A detailed review of AM applications in hybrid propulsion systems is given in Refs. [28,29]. The studies by Whitmore et al. [25,26] demonstrated the feasibility of FDM-printed polymeric fuels and the use of complex port geometries to enhance $\dot{r}_f$. Focusing on paraffin-based formulations, McCulley [30] fabricated porous ABS structures later filled with wax, while Lyne et al. [31] and Armold [32,33] investigated heterogeneous paraffin/acrylic configurations featuring honeycomb-like cells and non-conventional port designs. Although some of these heterogeneous grains achieved $\dot{r}_f$ and combustion efficiencies comparable to cast paraffin, issues including incomplete wax combustion and fuel expulsion were reported. More recently, Cai et al. [34] presented the use of FDM-printed structures to obtain throttleable performance from solid fuels, further highlighting the potential of AM for tailoring internal ballistics. The concept of embedding 3D-printed structures into paraffin grains has been further developed by the FDM-based *armored grain* concept introduced by Bisin et al. [11,14,35,36]. In this approach, paraffin wax is reinforced by cellular structures (gyroids) at different volume fractions and with different printing materials. This makes the fuel grain heterogeneous, with regions occupied by the 3D-printed skeleton and regions of neat paraffin matrix. The gyroid, a TPMS identified by Schoen [37], is particularly attractive as a reinforcing structure because it offers an efficient compromise between mechanical reinforcement and open volume, potentially preserving the ballistic performance of the wax. Other research groups have proposed related reinforcement concepts. Hill et al. [38] investigated paraffin slabs embedding PLA gyroids in both slab and hybrid motor configurations, observing complex effects on regression efficiency and $\dot{r}_f$. Nylon-12 scaffolds produced by selective laser sintering (SLS) were used by Zdybal et al. [39] to support polyethylene-wax/EVA emulsions, aiming at reducing the polymer content required for structural performance. Bresler and Natan [40] examined ABS skeletons enclosing paraffin, reporting regression rate enhancements attributed to recirculation zones generated by the slowly burning skeleton. Recently, efforts on the use of metallized thermoplastics for the printing of cellular structures are discussed by Rontini et al. [41], with the inclusion of micron-sized Al in ultraviolet radiation curing-printed structures.

3. Methodology

The objective of the work is to quantify how the architecture of the 3D-printed reinforcement affects the mechanical integrity and the $\dot{r}_f$ of the armored grain. Thus, the investigation combines (i) pre-burning analyses (thermal and mechanical properties investigation), (ii) structural simulations (FEA), and (iii) lab-scale firing experiments.

The workflow starts with the armored grain production. Being the grain-manufacturing process based on die-casting, compatibility of the melt fuel matrix with the scaffold structure must be verified first. A detailed wettability analysis is performed in Ref. [11], where macro-crystalline wax is identified as compatible with PLA. Yet, thermal behavior characterization is required for the paraffin and the polymer of the reinforcing structure to assess material compatibility during casting. This check is performed by thermal analysis (simultaneous differential thermal analysis (DTA)-thermogravimetry (TG)). The DTA-TG traces of wax and 3D-printing polymer are used to define a casting temperature window to avoid scaffold structure softening/deformation. Thanks to thermal analysis, degradation onset and end and peak temperatures of the materials can be determined. Following this step, mechanical characterization of reinforcing structures and armored grains is performed. Quasi-static compression is considered as the representative test for the analysis, since the primary loads in an engine operating phase are due to pressure and to standardize heterogeneous fuel treatment. While the considered load cannot be fully representative of the actual load conditions of grains during operations, the targeted relative grading of structures is made along their longitudinal axis. The behavior of cellular structures is studied first, then armored grains are considered. The experimental investigation of the mechanical response of different structures aims at identifying Young's modulus (E), and the stress and strain at yield (σ_y and ϵ_y, respectively) and is combined with FEA simulations to compare the stress/strain distribution in the structures. Finite element analyses assess armored grain behavior, using a simplified cubic unit to isolate architecture-driven load transfer effects. Finally, relative ballistic grading of the fuels is achieved, by a lab-scale HRE. In this phase, the $\dot{r}_f$ is considered as the main observable parameter of interest.

4. Materials and methods

4.1. Materials and tested fuels

4.1.1. Paraffin matrix and 3D printer polymer

A macro-crystalline paraffin wax (J1) is tested. The fuel matrix is composed of pure J1, loaded with 1 wt% of graphite powder (CP). The opacifier prevents in-depth radiation penetration during combustion. The J1 has a density of 0.91 $\mathrm{g/cm^3}$. PLA is selected as the printing material for the reinforcing structures. This choice is due to the good compatibility (i.e., wettability [11]) and overall thermal properties for this polymer [11]. In addition to this, PLA is easily printed by FDM [42]. The PLA is a thermoplastic aliphatic polyester derived from renewable biomass. Thus, it can be considered as a *green material*. The PLA filament used in the present study has a nominal density of 1.26 $\mathrm{g/cm^3}$.

4.1.2. 3D-printed reinforcing structures

The GY and the SP are TPMS structures. Honeycomb-based reinforcements are identified as straight and twisted honeycombs (SH and TH, respectively). The TPMS structures are built via the periodic repetition in space of the corresponding unit cell. Defining L as the side length of the cubic unit cell in which the individual cells are inscribed, the unit cells of GY and SP are described, respectively, byEqs. (1) and Eq. (2) [43]:

$$\sin\left(\frac{2\pi x}{L}\right)\cos\left(\frac{2\pi y}{L}\right)+\sin\left(\frac{2\pi y}{L}\right)\cos\left(\frac{2\pi z}{L}\right)+\sin\left(\frac{2\pi z}{L}\right)\cos\left(\frac{2\pi x}{L}\right)=0 \tag{1}$$

$$\cos\left(\frac{2\pi x}{L}\right)+\cos\left(\frac{2\pi y}{L}\right)+\cos\left(\frac{2\pi z}{L}\right)=0 \tag{2}$$

In the Eq. (1) and in the Eq. (2), L is the unit cell size of the cube the single GY and SP cells can be inscribed in (see Fig. 1(a) and (b)). In actual GY and SP solids, a printed layer thickness (d) is associated to the surface to create the cellular solid. In the analysis, d is equal to the diameter of the printer nozzle. For a given L, the surface-to-volume ratio of the structures is higher for the GY than for the SP. For the honeycomb structures, L denotes the side length of the hexagonal core cell shown in Fig. 1(c). The TH cells feature a sweep of 1/4 turns per inch (TPI) along the cylinder axis. This choice is taken to provide an artificial swirl component to the flow in the port to enhance propellant mixing and heat transfer to the surface. A detailed analysis of the swirl level is out of the scope of the work, that aims at contrasting different TPMS architectures with more conventional structures. Detailed analyses on the effects of induced swirl in 3D-printed grains without and with paraffin matrix are reported in Refs. [32,33,44].

For all the considered geometries (GY, SP, SH, TH), the L parameter is the responsible for the volume fraction of the reinforcing structures. In the present work, volume fraction, infill, and relative density ($\tilde{\rho}_{\%}$) are used interchangeably to indicate the same property. The $\tilde{\rho}_{\%}$ is defined as the ratio between the density of the structures (the reinforcing structure mass divided by the enveloped volume) and the density of the solid material (i.e., PLA). The investigated structures are listed in Table 1 and shown in Figs. 2 and 3. Three gyroids featuring different relative densities are considered to inspect the effect of the $\tilde{\rho}_{\%}$ on the mechanical properties of the structure itself. The influence of the topology was studied contrasting the reinforcements with the same $\tilde{\rho}_{\%} \approx 15\%$ (see Table 1).

The reinforcements were printed employing a commercial FDM 3D printer (Prusa i3 MK3). A 0.4 mm extruder nozzle was used, and the printer layer height was set to 0.2 mm. The structures were cylindrically shaped, as shown in Figs. 2 and 3, to be consistent with previous studies [11]. The design process of the GY specimens exploited the infill pattern of the native (open-source) slicer of the printer. Details on the production of the gyroids are reported in Bisin et al. [11]. The SP samples were produced starting from the Eq. (2) and setting the L value to 6.5 mm. The related surface is generated in MATLAB and then thickened according to the extrusion width of the 3D printer (0.4 mm extruder nozzle). A similar approach was employed for the SH and TH: the length side of the hexagonal cell was selected (L = 3.2 mm), and the final structure generated by a CAD software (Autodesk Inventor).

4.1.3. Armored grains

The armored grains are manufactured via melt casting: the 3D-printed reinforcing structure is inserted in a mold. The melted paraffin is then poured into the mold. Casting is performed in a temperature window that provides a sufficiently low melt viscosity, while limiting thermal softening of the 3D-printed PLA structure (i.e., glass transition temperature). Armored grains show structural integrity after casting, preserving their nominal sizes, with 30 mm diameter and 50 mm length. In addition to this, density of the samples is close to the theoretical maximum density, with deviations below 5%. The investigated armored grains are summarized in Table 2. The effect of the GY infill on the mechanical properties was assessed testing different relative densities. The

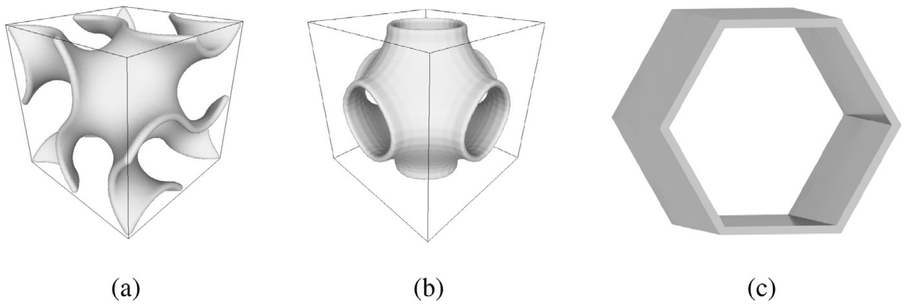

Fig. 1. Unit cells of the considered reinforcing structures: (a) gyroid, (b) Schwarz-P and (c) honeycomb.

Table 1
Investigated structures. Printing parameters: (i) nozzle diameter of 0.4 mm, (ii) print layer height of 0.2 mm, (iii) characteristic unit-cell size L, ranging from 7 to 15 mm for the gyroids and equal to 6.5 mm and 3.2 mm for the Schwarz-P and honeycomb structures, respectively. Nominal and actual $\tilde{\rho}_{\%}$ are reported per each structure.

Specimen	Structure	Parameter, L (mm)	Nominal relative density, $\tilde{\rho}_{\%}$ (%)	Actual relative density, $\tilde{\rho}_{\%}$ (%)	Notes
GY_i07	Gyroid (GY)	15.0	7	7.8 ± 0.1	
GY_i10	Gyroid (GY)	10.5	10	10.2 ± 0.1	Infill effects
GY_i15	Gyroid (GY)	7.0	15	14.6 ± 0.1	
SP_i15	Schwarz-P (SP)	6.5	15	14.8 ± 0.1	
SH_i15	Straight honeycomb (SH)	3.2	15	15.5 ± 0.1	Topology effects
TH_i15	Twisted honeycomb (TH)	3.2	15	15.4 ± 0.1	

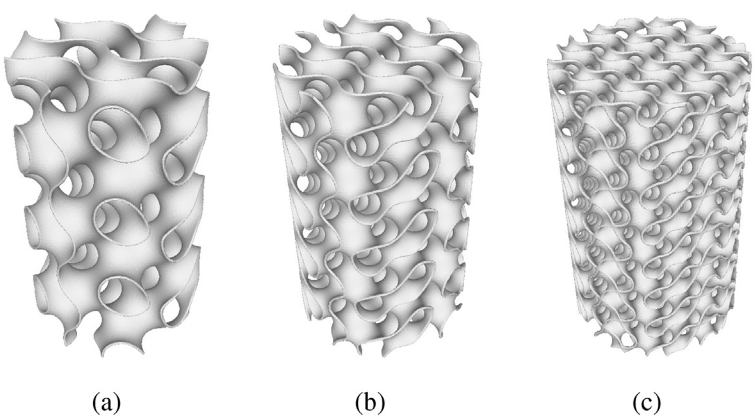

Fig. 2. Investigated GY-based reinforcements with (a) 7%, (b) 10% and (c) 15% infill (GY_i07 to GY_i15 respectively). Actual relative densities are reported in Table 1. Specimen sizes: 30 *mm* in diameter and 50 *mm* in height.

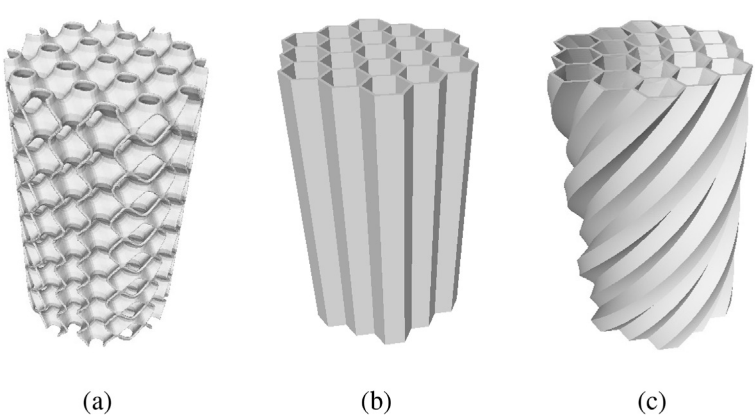

Fig. 3. Investigated non-GY-based reinforcing structures featuring 15% infill: (a) SP_i15, (b) SH_i15 and (c) TH_i15. Actual relative densities are reported in Table 1. Specimen sizes: 30 *mm* in diameter and 50 *mm* in height.

influence of the geometry on the armored grain mechanical behavior was investigated contrasting GY, SP, SH, TH with 15% infill.

4.2. Methods

4.2.1. Pre-burning analyses

Pre-burning analyses of the tested ingredients are performed by simultaneous thermal analysis, viscosity determination under reference conditions, and compression testing for mechanical properties assessment.

DTA-TG tests are performed in Ar (70 ml/min) with heating rate of 10 K/min. The main observable parameters of interest are the temperatures for onset and end of the thermal degradation (T_{On}, and T_{End}), and the temperature of the melting peak (T_{Peak}). Onset and end temperatures are determined by tangent's method [11]. The viscosity of the paraffin wax is determined by a plate-plate configuration, when operat-

Table 2
Investigated armored grains. Macro-crystalline wax (J1) is reinforced with gyroids featuring infills in the range 7 to 15%, while different reinforcement topologies are contrasted for a nominal infill of 15%.

Specimen	Armored grains components		TMD,	Notes
	Paraffin waxes	Reinforcement	ρ_f (g/cm^3)	
J1_GY_i07	J1	GY_i07	0.93	Infill effects
J1_GY_i10	J1	GY_i10	0.94	
J1_GY_i15	J1	GY_i15	0.96	
J1_SP_i15	J1	SP_i15	0.96	Topology effects
J1_SH_i15	J1	SH_i15	0.96	
J1_TH_i15	J1	TH_i15	0.96	

Table 3
Mechanical properties of the J1 paraffin and PLA (compression rate 1 *mm/min*, testing temperature 298 ± 5 *K*). For J1 manufacturing, die-casting is considered, while PLA cylinders with 100% infill are printed.

Specimen	Young modulus, E (MPa)	Yield stress, σ_y (MPa)	Yield strain, ϵ_y (%)	Density, ρ (g/cm^3)
J1	264 ± 51	1.87 ± 0.12	0.94 ± 0.08	0.911 ± 0.01
PLA	2349 ± 64	68.48 ± 2.54	4.34 ± 0.20	1.258 ± 0.01

ing above the melting temperature of the alkane, at 423 K. Shear rates from 10 to 1000 s^{-1} are investigated, with the latter value taken as convenient reference [13]. Uniaxial compression tests are carried out on the reinforcing structures and on the armored grains according to the ISO 604 [45]. An MTS 810 universal testing machine equipped with a 250 kN load cell was used. The compression tests were conducted at ambient temperature (T = (298 ± 5) K) with compression rate of 1 mm/min. Four samples were tested per each specimen type. The norm does not impose any specific specimen size or shape. Therefore, the specimen was shaped as a cylinder with base diameter of 30 mm and height of 50 mm (the same external dimensions used for the ballistic characterization). Data for the compression tests are evaluated as engineering stresses [11].

4.2.2. Finite element analysis (FEA)

The aim of the numerical simulations is to investigate the use of FEA to improve the interpretation of the mechanical behavior of the reinforcing structures and of the armored grains. The employed software for FEA is Femap with NX Nastran [46,47]. The simulations focus on the compression tests and replicate the same operating conditions considered for the experimental campaign. Independently from the kind of simulation (reinforcing structure only/complete armored grain), FEA implementation consisted of the following steps: (i) creation of the mesh, (ii) definition of the elements and of the materials, (iii) setting of loads and constraints. The FEA meshes of GY and SP were created exploiting the Eqs. (1) and (2), the periodicity of the structures, and the repetition of the unit cells (refer to Fig. 1, and Ref. [48] for details). The final meshes involved 2D plate elements (Nastran CTRIA), whose thickness was set to the extrusion width of the 3D printer. The mesh density impact on the FEA results was investigated considering the gyroid unit cell with L = 8.25 mm as reference case. The PLA was chosen as material and the 2D meshes exploited triangular CTRIA3 elements with thickness set to 0.45 mm. Six different meshes with different numbers of elements (800, 1200, 1600, 2400, 3200, 4000) were created. The respective results are reported in Section 5.2. The CAD models of the honeycomb-like structures (SH, TH) were used as input geometries for the FEA, and solid elements (CTETRA) were selected for the analysis. In all the simulations, two rigid elements (RBE2) were created and connected to the top and bottom nodes of the sample to model the contact plates of the compression test rig. An enforced displacement was prescribed to the rigid element at the top to simulate the compression imposed by the machine. The employed solver was SOL106 (non-linear, static) [49]. Compression tests performed on the 3D-printed PLA specimens allowed the definition of the material properties (reported in Table 3). A preliminary FEA investigation was also conducted on the armored grains featuring the GY reinforcements at different infill percentages (7%, 10%, 15%). In the modeling approach, the (cylindrical) armored grain is split into the two components: the paraffin matrix (J1) and the GY reinforcement (PLA). The GY surface divides the surrounding paraffin waxes in two complementary continuous phases. Solid elements with the mechanical properties of the J1 (listed in Table 3) were used to model the paraffin matrix (both the continuous phases, see Fig. 4).

As a first approximation, the paraffin-gyroid interface was modeled as a glue contact [46]. However, the numerical simulations focused on the smallest repetitive (and representative) unit of the armored grain, hereafter referred to as *armored cube*. This choice was made to reduce the computational cost, while preserving the purpose of the analysis (i.e., inspecting the effect of $\tilde{\rho}_{\%}$ on the mechanical properties of the armored grains). Three different GY-armored cubes, featuring the three different relative densities (7%, 10%, 15%), were considered. The length of the armored cubes corresponds to the gyroid unit cell size L (see Table 1). More specifically, the armored cubes with nominal $\tilde{\rho}_{\%}$ at 7%, 10%, 15% feature L values equal to 15 mm, 10.5 mm, 7 mm, respectively.

4.2.3. Burning analyses

The relative ballistic grading of the fuel formulations is carried out on a lab-scale hybrid engine at the SPLab, based on the $\dot{r}_f$. The facility is fully described in Ref. [14]. The study focuses on armored grains featuring structures with 15% relative densities (refer to specimens J1_XX_i15, in Table 2). The facility is designed to burn single-perforated cylindrical grains in a vertical configuration. The specimens feature a 5 mm port diameter, and a geometry similar to that of the compression tests (see Section 4.2.1). Combustion tests are performed in gaseous oxygen (GOX) with an initial oxidizer mass flux (G_{ox}) of 250 kg/(m^2 · s). The oxidizer mass flow rate was regulated by a digital flowmeter and set to 5 g/s. The pressure trace recorded during the burning test was analyzed to retrieve the combustion duration $\Delta t_b = t_{end} - t_{in}$. In particular, t_{end} coincides with the injection of the gaseous nitrogen to quench the combustion, whereas t_{in} is chosen as the time at which the chamber pressure reaches 70% of the maximum value during the firing. The burning time

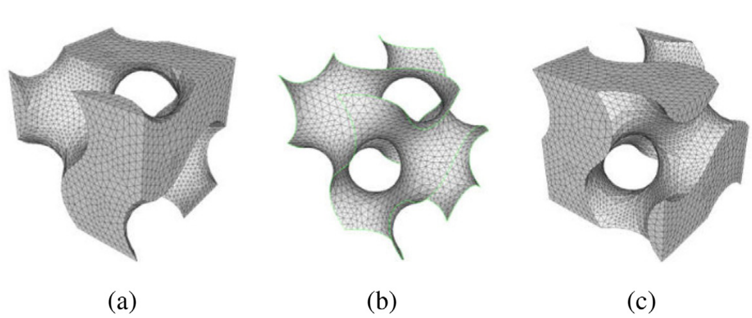

Fig. 4. Individual components used in the FEA model of GY-armored grains: (a, c) paraffin matrix domains and (b) gyroid structure. Components (a) and (c) are complementary, with the gyroid conforming to the interface between the two paraffin blocks.

Table 4
Mechanical properties of reinforcing structures (compression rate 1 *mm/min*, testing temperature 298 ± 5 *K*).

Specimen	Young modulus, E (MPa)	Yield stress, σ_y (MPa)	Yield strain, ϵ_y (%)	Density, ρ (g/cm^3)	Relative density, $\tilde{\rho}_{\%}$ (%)
GY_i07	31 ± 2	0.69 ± 0.06	2.53 ± 0.23	0.09 ± 0.00[a]	7.8 ± 0.1
GY_i10	60 ± 3	1.50 ± 0.04	3.11 ± 0.08	0.12 ± 0.00[a]	10.2 ± 0.1
GY_i15	109 ± 1	2.96 ± 0.01	3.89 ± 0.12	0.18 ± 0.00[a]	14.6 ± 0.1
SP_i15	50 ± 2	1.42 ± 0.04	4.89 ± 0.09	0.18 ± 0.00[a]	14.8 ± 0.1
SH_i15	433 ± 4	9.73 ± 0.26	2.99 ± 0.13	0.19 ± 0.00[a]	15.5 ± 0.1
TH_i15	223 ± 7	4.60 ± 0.28	2.81 ± 0.14	0.18 ± 0.00[a]	15.4 ± 0.1

[a] Over three measurements, the confidence interval is < 0.01.

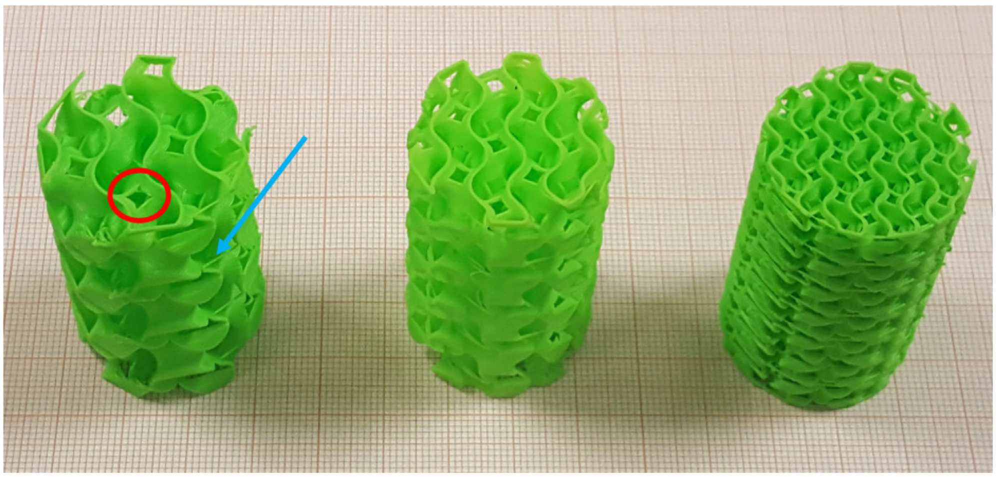

Fig. 5. 3D-printed PLA gyroids with 7%, 10%, 15% nominal infill (from left to right). Specimen sizes: 30 mm in diameter and 50 mm in height. Red circles and blue arrows show saddle points and printing defects, respectively, on the 7% gyroid. These defects are visible also in the 10% and 15% structures (reprinted from Acta Astronautica, Vol. 176, R. Bisin, C. Paravan, S. Alberti, L. Galfetti, A new strategy for the reinforcement of paraffin-based fuels based on cellular structures: The armored grain - Mechanical characterization, pp. 494-509, Copyright (2020), with permission from Elsevier - see Ref. [11]. Current gyroids share the printing device and procedure).

was set to 4–5 s, depending on formulation ballistic response (to provide similar conditions during the runs).

To compute the solid fuel regression rate $\dot{r}_f$, the mass-based (MB) method is used. The MB is a thickness over time approach, the $\dot{r}_f$ is calculated as:

$$\dot{r}_{f,MB} = \frac{\Delta m_b}{\rho_f \cdot \overline{A}_b \cdot \Delta t_b} \tag{3}$$

where Δm_b represents the difference between the mass of the specimen before $(t = t_{in})$ and after the combustion $(t = t_{end})$, ρ_f is the density of the fuel, and $\overline{A}_b$ is the average burning area that can be evaluated as:

$$\overline{A}_b = \pi \cdot \frac{D(t_{in}) + D(t_{end})}{2} \cdot H \tag{4}$$

In the Eq. (4), H is the grain length before the firing, $D(t_{in})$ and $D(t_{end})$ are the port diameter before and after the combustion test, respectively.

The average oxidizer mass flux of the test is defined as the oxidizer mass flow rate $(\dot{m}_{ox})$, divided by the average port area:

$$\overline{G}_{ox} = \frac{16 \cdot \dot{m}_{ox}}{\pi \cdot \left[D(t_{end}) + D(t_{in})\right]^2} \tag{5}$$

5. Results and discussion

5.1. Pre-burning analyses

Thermal analyses on the J1 show an initial melting, with $T_{peak,1} = 320$ K, followed by a second melting peak at $T_{peak,2} = 339$ K and a thermal degradation process with $T_{On} = 532$ K and $T_{End} = 603$ K. A mass loss of 2% is achieved by the wax at a temperature of 485 K. For PLA, a glass transition temperature is observed at 335 K, with $T_{peak} = 424$ K, while T_{On} and T_{End} are 620 K and 652 K, respectively. Rheological analyses on the J1 loaded with CP reveal a viscosity of 0.002 Pa·s at 1000 s^{-1}, with no significant changes over the investigated shear-rate range. Mechanical properties of the raw components of the armored grains are listed in Table 3.

The manufacturing process of reinforcement structures introduces surface defects, as shown in Figs. 5, 6, 7, and partially discussed also in Ref. [35]. These defects affect the behavior of the different structures and possibly their responses during mechanical tests. Typical compression tests on reinforcing structures are shown in Fig. 8. The mechanical results for TPMS and honeycombs are shown in Table 4, while the mechanical behaviors of the different structures are displayed in Fig. 9. Table 4 highlights a connection between higher $\tilde{\rho}_{\%}$ and stronger mechanical properties, in terms of stiffness, strength and elastic limit enhancement. This is consistent with scaling laws connecting mechanical properties and $\tilde{\rho}_{\%}$ [50]. Considering the GY specimens in Fig. 9(a), the stress-strain curves initially feature a linear part up to the elastic limit and then a yield point (ϵ_Y, σ_Y). After that threshold, the structure collapses at nearly constant stress till densification is achieved (note that this is not reached in the considered interval). The collapsing mechanism of the GY is visible in Fig. 8(a). The GY responds to compression by crumpling constantly and homogeneously. The struts of the GY buckle near the compression plates. This might be due to manufacturing defects in the bottom and upper print layers (see Fig. 6(a)). The stress-strain curve of GY samples and the collapsing mechanism suggest a bending-dominated nature [50].

Fig. 9(b) allows a comparison between the mechanical behavior of different structures with the same relative density (and the same mass, given the operating conditions). The honeycomb-like structures (SH_i15 and TH_i15) exhibit higher σ_Y than the TPMS counterparts (GY_i15 and SP_i15). On the other hand, SH_i15 and TH_i15 show a sudden fall of the stress after the yield point. The TPMS with 15% infill feature a plateau stress closer to the yield stress value. These behav-

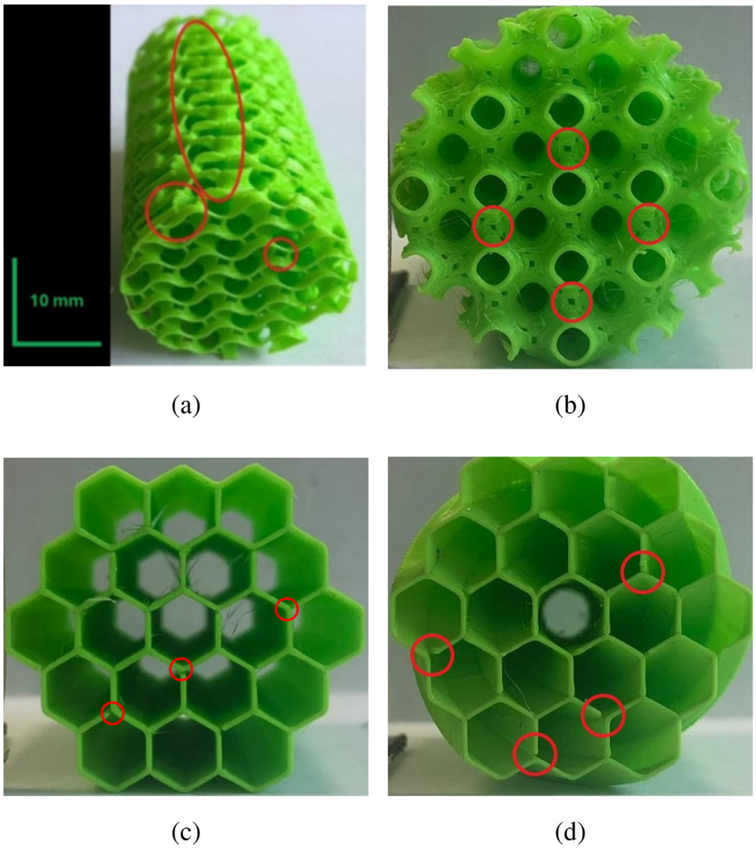

Fig. 6. Top view of 3D-printed PLA structures with 15% nominal infill: (a) GY_i15, (b) SP_i15, (c) SH_i15, and (d) TH_i15. Red circles show printing defects characterizing each structure. Note that in (b), (c) and (d) the printed part maximum width is 30 *mm*.

iors for honeycombs and TPMS structures highlight the different nature of the two classes of architectures: the bending-dominated GY_i15 and SP_i15 structures, and the stretch-dominated SH_i15 and TH_i15. Bending-dominated structures are well suited to absorb energy under compression, whereas the stretch-dominated structures are exceptionally stiff and strong. Fig. 8(b) shows the collapsing mode of the SH: the specimen initially withstands the load with small strains, then the cells start to open and a brittle fracture occurs, as testified by the drop in the stress-strain curve. The honeycomb-like samples (SH_i15 and TH_i15) abruptly fractured after the yield point (see Fig. 9(b)). This is related to the mechanism of deformation of stretch-dominated structures, whose struts undergo tension and compression, rather than bending. For SH_i15, printing defects along honeycomb cells longitudinal extension may affect the mechanical response, as suggested by the analysis of Figs. 7 and 8(b). The SP_i15 features the lowest values of E and σ_y in the dataset, under the investigated conditions. The stiffness and the strength of SP_i15 are half of those of GY_i15. The printing process could have had an impact on the mechanical properties, especially for the SP_i15 specimens. In fact, during the printing process, the nozzle does not always follow a continuous and well-defined path, leading to possible flaws and imperfections. Actually, each structure shows minor printing defects (see Fig. 6). Comparing GY_i15 (Fig. 6(a)) and SP_i15 (Fig. 6(b)) structures, the larger number of voids and printing imperfections characterizing the SP structure may be linked to the mechanical properties offset between the two TPMS.

Thus, an improvement of the printing process could lead to enhanced mechanical properties of the SP_i15. Finally, the TH_i15 exhibits σ_y and E greater than those of the SP_i15 and GY_i15. Yet, the performance of the twisted honeycomb structure is lower than that of the SH_i15 (see Table 4), when maximum σ_y and ϵ_y are considered. This behavior may be due to the twisting that made the honeycomb behave as a mixed bending- and stretch-dominated structure. The printing defects of the TH_i15 may play a role in the mechanical response of the system being mainly located along the twisting honeycomb connections, see Fig. 7.

Table 5
Mechanical properties of armored grains (compression rate 1 *mm/min*, testing temperature 298 ± 5 *K*).

Specimen	Young modulus, E (MPa)	Yield stress, σ_y (MPa)	Yield strain ϵ_y (%)
J1	264 ± 51	1.87 ± 0.12	0.94 ± 0.08
J1_GY_i07	210 ± 29	2.14 ± 0.06	4.01 ± 0.24
J1_GY_i10	260 ± 37	3.07 ± 0.06	4.14 ± 0.17
J1_GY_i15	262 ± 66	4.72 ± 0.12	4.26 ± 0.48
J1_SP_i15	154 ± 22	2.08 ± 0.07	4.42 ± 0.44
J1_SH_i15	323 ± 29	8.19 ± 0.32	2.91 ± 0.11
J1_TH_i15	234 ± 26	4.48 ± 0.17	4.32 ± 0.23

Fig. 10 shows compression tests on selected armored grains (GY and SH). Fig. 11 reports the stress-strain curves of the investigated armored grains, while Table 5 shows a summary of the relevant data (E, ϵ_y and σ_y). The effect of the $\tilde{\rho}$ on the mechanical properties of the armored grains follows a trend observed for the structures alone (Fig. 9(a)): augmented mechanical properties at compression are achieved as the infill increases. The GY-armored grains present an elastic field that mainly depends on the J1 paraffin properties, and a plastic field driven by the structures. Table 5 shows that the E values of the GY-armored grains are similar to each other and to the one of J1. Instead, the strength of the fuels is influenced by the $\tilde{\rho}_{\%}$ of the embedded GY-reinforcement. These results confirm the findings for armored grains based on microcrystalline wax-reinforced by GY [11]. The J1_GY_i07, J1_GY_i10, and J1_GY_i15 led to increases of 14%, 64%, and 152% of σ_y with respect to the J1. Fig. 11(a) shows a change in the slope of the stress-strain curve near the yield strain value of the pristine J1 paraffin. The stress-strain curves suggest that the paraffin drives the behavior of the armored grain

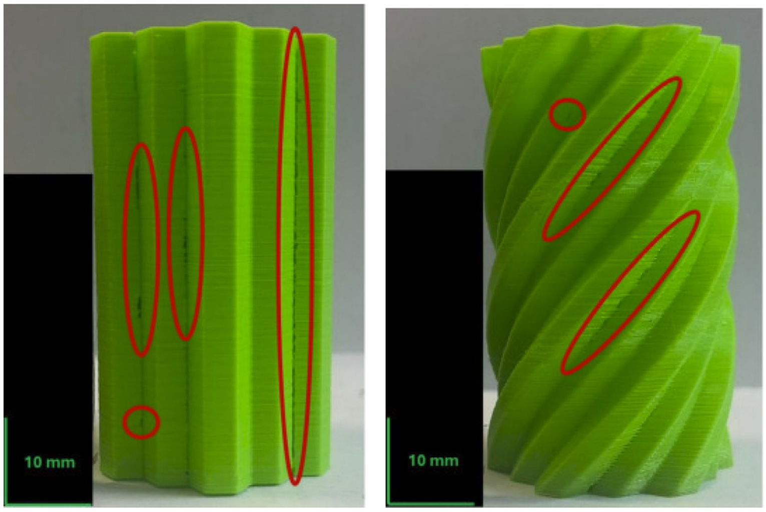

(a) (b)

Fig. 7. Side view of 3D-printed reinforcing structures: (a) SH_i15 and (b) TH_i15. Printing defects are highlighted.

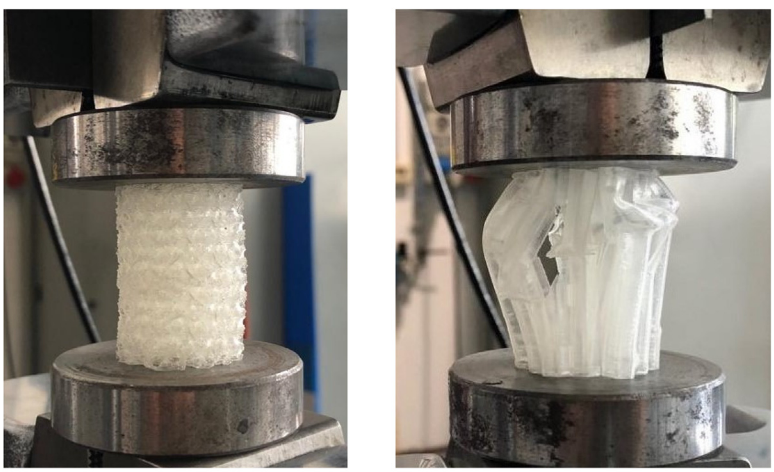

(a) (b)

Fig. 8. Reinforcing structures during compression test: (a) GY_i15 and (b) SH_i15 (compression rate of 1 *mm/min* and testing temperature of 298 ± 5 *K*).

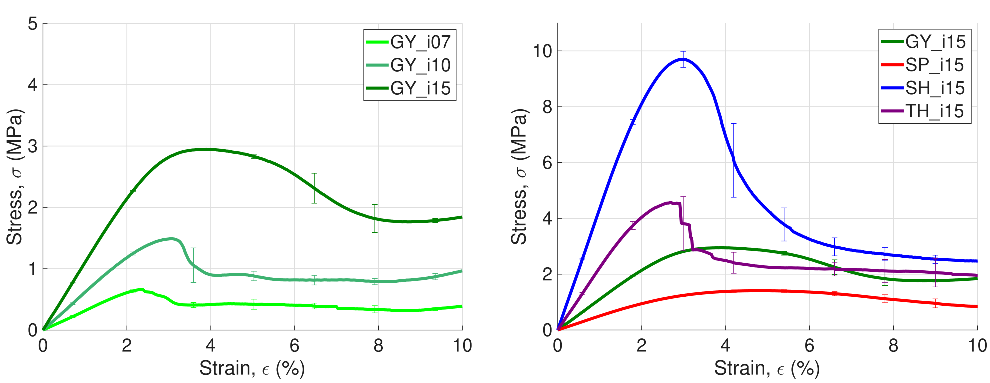

(a) (b)

Fig. 9. Engineering stress-strain curves of (a) gyroids and (b) 15% infill reinforcing structures. The curves represent ensemble averages obtained at compression rate of 1 *mm/min* and testing temperature of 298 ± 5 *K*.

until its yield point (coinciding, for J1 with the failure point), then, the structure prevails and helps the paraffin to withstand the load, increasing the overall σ_y of the armored grain. Once the sample enters the plastic field, the armored grain behaves like the reinforcing structure with a flat and long plateau stress, whose value depends on the embedded GY. As shown in Fig. 11(a), the real breakthrough of the GY-armored grains is that the brittle behavior of the J1 fuels turned into a ductile one, regardless of the GY exploited as reinforcement. Moreover, the yield point of GY-armored grains is no longer the failure point, unlike the J1. Fig. 11(b) shows the mechanical behavior of J1 fuels reinforced with the 15% infill structures. All the armored grains show increased σ_y and strain energy, avoiding the typical brittle behavior of the paraffin-based fuel. Comparing the different geometries, the armored grains based on TPMS structures exhibit lower E and σ_y, thus reflecting the results in

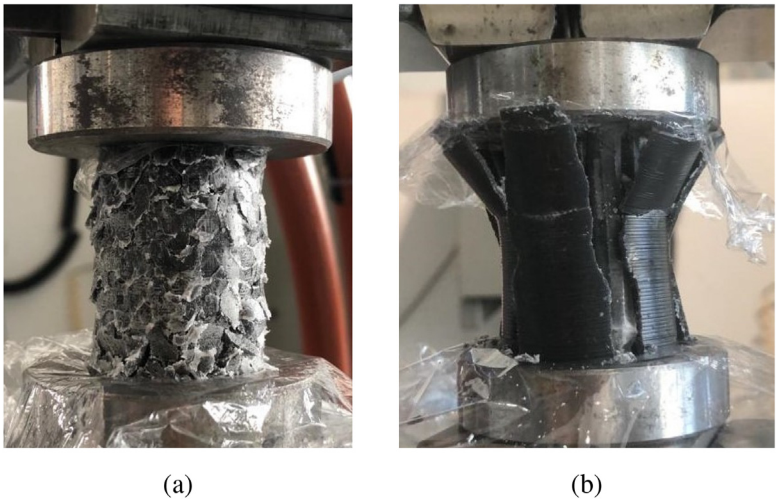

Fig. 10. Armored grains during compression testing: (a) J1_GY_i15 and (b) J1_SH_i15 (compression rate of 1 *mm/min* and testing temperature of 298 ± 5 *K*).

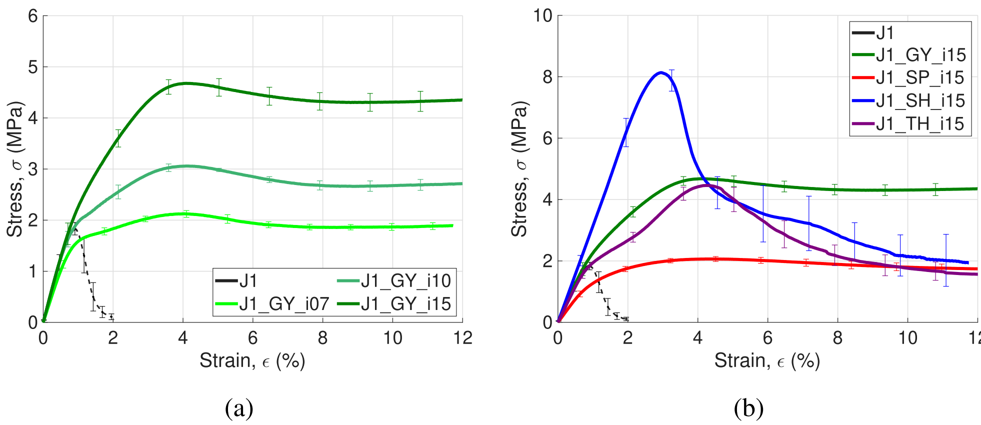

Fig. 11. Engineering stress-strain curves of (a) GY-based armored grains and (b) 15% infill armored grains. The curves represent ensemble averages obtained at compression rate of 1 *mm/min* and testing temperature of 298 ± 5 *K*.

Fig. 9(b). The GY- and SP-armored grains feature a plateau stress after the yield point, whereas the SH- and the TH- exhibit a drop after this point (see Figs. 9(b) and 11(b)). Under the investigated conditions, J1_SH_i15 and J1_TH_i15 exhibit σ_y and E comparable with those identified for the reinforcing structures alone. Conversely, the mechanical properties of GY- and SP-armored grains are greater, not only in comparison with the J1 paraffin fuel, but also of the ones of the reinforcing structures. The J1_TH_i15 exhibits a change in the slope of the stress-strain curve near the yield point of the J1 paraffin, as the J1_GY_i15. Under the investigated manufacturing and testing conditions, the J1_SP_i15 exhibits a lower E than the pure paraffin. A likely explanation for the behavior is given by the mechanical properties of the structure alone (see Fig. 9(b) and Table 4), and by the lower surface to volume ratio of the SP with respect to the GY. In Fig. 11(b), the standard deviation of the honeycomb-like structures results higher with respect to the one of the GY- and SP-armored grains, especially after the yield point. This can be attributed to the failure mode of these structures involving the honeycomb cell cracking and the release of paraffin fragments (Fig. 10).

5.2. Finite element analysis (FEA)

Table 6 shows the results of the mesh convergence study. Based on the analysis on mesh refinement, simulations were carried out using meshes with 1600 elements per gyroid unit cell.

This density provides a suitable combination of numerical accuracy and computational cost. Indeed, the mechanical properties of the 1600 CTRIA unit cells capture the E and σ_y characterizing the GY_i15 reinforcement structure (see Table 4). Interestingly, when passing from 800 to 1200 elements the stiffness and the strength of the gyroid rise

Table 6
Mechanical properties of FEA simulated gyroid unit cell with L = 8.25 *mm* and plate thickness of 0.45 *mm*: effect of mesh density (CTRIA3 elements). Percent differences of two consecutive analyses are indicated in brackets. The CPU time is evaluated as percent variation with respect to the (reference) 800 CTRIA3 case. Computational time is evaluated on an Intel i7 processor working at 3.6 GHz.

Elements	Young modulus, E (MPa)	Yield stress, σ_y (MPa)	CPU time difference, Δt_{CPU} (%)
800	108.5 (–)	3.04 (–)	–
1200	111.5 (+2.8%)	3.13 (+2.8%)	+20
1600	110.0 (−1.4%)	2.93 (−6.2%)	+77
2400	108.6 (−1.3%)	2.90 (−1.3%)	+158
3200	107.3 (−1.2%)	2.76 (−4.8%)	+213
4000	107.1 (−0.3%)	2.71 (−1.5%)	+232

(+ 2.8%), then the trend is reversed with denser meshes. The latter exhibit (small) E and σ_y reductions. The E is almost unchanged when using 4000 elements instead of 3200 (−0.3% difference). On the contrary, the σ_y is characterized by a relatively larger variation (1.5%). It is noteworthy that the size of the element has an impact on the early failure of the analysis: denser meshes seem to fail at an earlier strain value compared to the coarser counterparts, see Fig. 12. Denser meshes feature smaller elements, that - under compression - are exposed to higher deformation and are more prone to reach the maximum allowable value for each element.

Table 7 summarizes the relevant numerical FEA results. The von Mises stress distributions in GY_i07 and TH_i15 are reported in Fig. 13.

Table 7
Mechanical properties of FEA simulated reinforcing structures.

Specimen	Young modulus, E (MPa)	Yield stress, σ_y (MPa)	Yield strain, ϵ_y (%)	Density, ρ (g/cm^3)	Relative density, $\tilde{\rho}_{\%}$ (%)
GY_i07	41	1.14	3.31	0.09	7.9
GY_i10	73	2.18	3.28	0.14	11.4
GY_i15	126	3.65	3.08	0.21	17.4
SP_i15	70	1.97	3.12	0.19	15.9
SH_i15	372	10.43	3.26	0.18	15.4
TH_i15	247	7.6	3.56	0.18	15.4

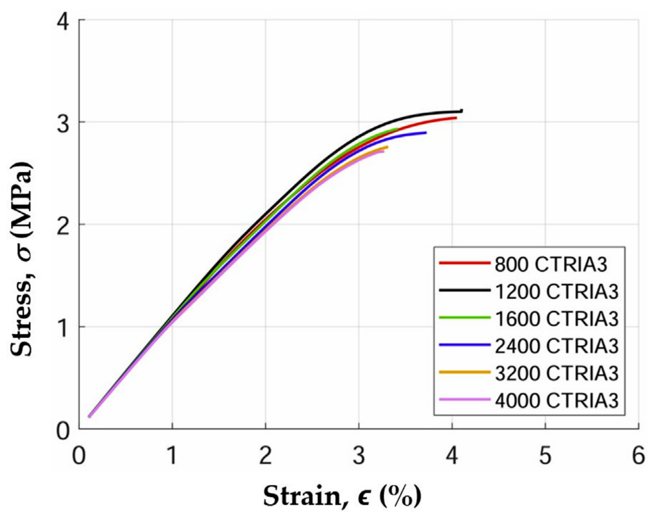

Fig. 12. FEA stress-strain curves of the gyroid unit cell with L = 8.25 *mm*: effect of mesh density. Meshes of triangular CTRIA3 elements with plate thickness of 0.45 *mm*.

The two structures are selected for clarity in their visualization. The gyroid (see Fig. 13(a)) exhibits a complex stress distribution with the highest values localized in the areas where the struts start bending. Fig. 13(b) highlights a stress concentration near the external surface of the honeycomb and a stress distribution following the sweep of the honeycomb channels. The stress location reveals that the TH_i15 could collapse due to both honeycomb cells cracking (stretch-dominated behavior) and struts bending. Focusing on the GY specimens, the results in Table 7 shows that the FEA captures the $\tilde{\rho}_{\%}$ impact on mechanical performance. Contrasting Tables 4 and 7, FEA overestimates the mechanical properties of the real structures. A first explanation for these differences is the higher $\tilde{\rho}_{\%}$ in GY models than in 3D-printed samples. Such a difference is more marked for GY_i10 and GY_i15, whose relative densities are 12% and 19% higher than those of the experimental models. The lower $\tilde{\rho}_{\%}$ is related to the presence of saddles in the 3D-printed specimens due to the discrete height difference of two consecutive layers, an effect discussed in detail in Bisin et al. [11]. A second explanation for the observed differences between experiments and FEA, is that to the fact that 3D-printing defects (such as poor layer-to-layer adhesion) are not captured by the simulations. The maximum mismatch is observed for the GY_i07: the FEA gyroid exhibits a +32% in E and +65% in σ_y with respect to the experimental counterpart. However, the increments of stiffness and strength for the FEA gyroids at different $\tilde{\rho}_{\%}$ are consistent with those of the 3D-printed gyroids. Numerical analysis supports the experimental findings about the stiffest and strongest structures for a given $\tilde{\rho}_{\%}$. In particular, TH_i15 shows an intermediate behavior between SH_i15 and GY_i15, as observed in the experimental test campaign. The FEA of SP_i15 returns higher E (+40%) and σ_y (+38%) than the 3D-printed specimen (Table 4). Conversely, a good agreement is found between FEA and experiments for SH_i15. This highlights that the 3D-printing process of SH specimens was less prone to produce defects and voids, as also testified by the match of $\tilde{\rho}_{\%}$ for the FEA and 3D-printed samples and the faint impact of major defects of the SH_i15 in compression test (see Figs. 6, 7).

Results of FEA performed on the *armored cubes* are listed in Table 8, while Fig. 14 shows the Von Mises stress distribution of the two components of the armored grains: the paraffin waxes and the gyroid re-

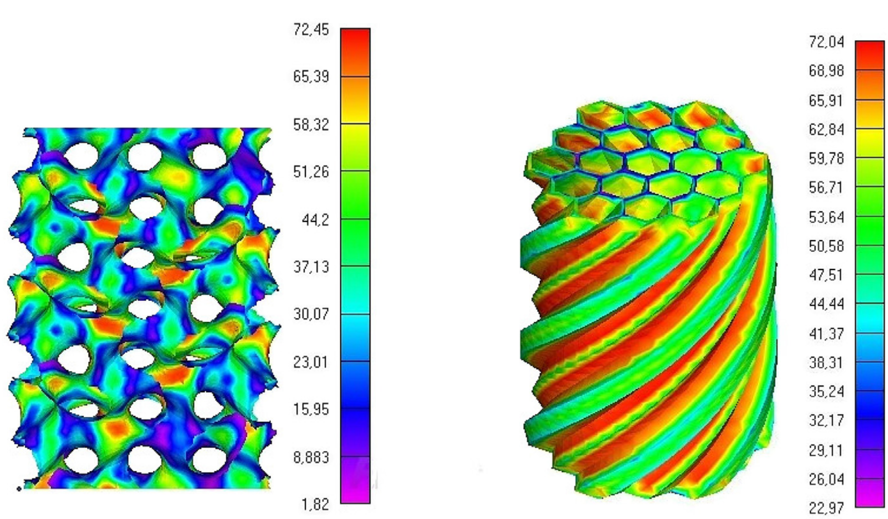

(a) (b)

Fig. 13. FEA of reinforcing structure: von Mises stresses (in MPa) at ϵ = 4% for (a) GY_i07 and (b) TH_i15.

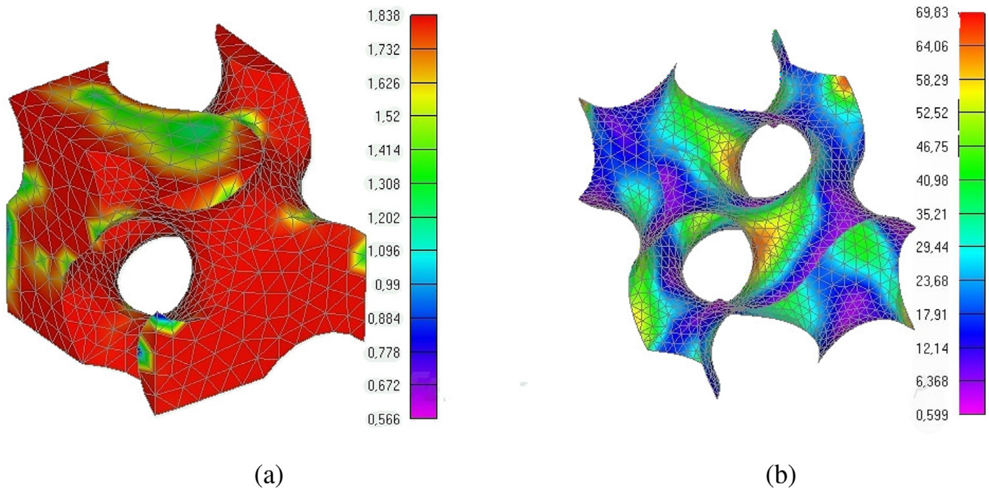

Fig. 14. FEA on J1_GY_i10_cube at $\epsilon = 2.5\%$: von Mises stresses (in MPa) for (a) paraffin matrix and (b) gyroid structure.

Table 8
Mechanical properties of FEA simulated *armored cube* featuring gyroid unit cells as reinforcements.

Specimen	Young modulus, E (MPa)	Yield stress, σ_y (MPa)	Yield strain ϵ_y (%)
J1_GY_i07_cube	371	3.51	5.46
J1_GY_i10_cube	396	4.07	5.11
J1_GY_i15_cube	434	5.05	5.33

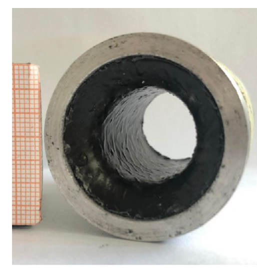

Fig. 15. Head-end view of the pure paraffin grain (J1) after the firing test; the oxidizer flow is directed into the page.

inforcement. The structural benefit of embedding denser gyroids with higher $\tilde{\rho}_{\%}$ is well captured by the results. The ϵ_y is nearly the same for the three armored cubes. For all the samples, the E is greater than that of the pure J1 ($E = 264$ MPa). The $\tilde{\rho}_{\%}$ change in the range 7 to 15% does not significantly alter the E of the simulated GY. The variation between FEA and experimental results in Table 5 is in the range +52% to +76%. A mismatch in the σ_y is noted when contrasting FEA and experiments. The maximum difference (+64%) is experienced with the armored grain featuring a 7% infill gyroid. These discrepancies may be attributed to the modeling approach adopted for the GY-armored grains. FEA gyroid and paraffin geometries were joined using the *Glue* function, which enforces a perfectly bonded interface. This represents a significant overestimation, as the interfacial slip occurring between the paraffin matrix and the reinforcement structure during deformation is neglected [11]. In spite of such a mismatch, the FEA analysis reveals insights on the effects of the armored grain, with the structure contrasting the critical breakage of the paraffin matrix under loads. Yet, on a relative grading, *armored cubes* enable identifying possible criticalities in the behavior of the armored grains (i.e., percent difference around 40% on E, though ϵ_y and σ_y are more scattered).

5.3. Burning analyses

An overview of the performed firing tests is given in Table 9, with $\dot{r}_f$ calculated based on the Eq. (3). In the dataset, conventional HTPB is considered for completeness. Regression rate enhancements of the fuels are evaluated considering J1 as a baseline. The pristine macro-crystalline paraffin shows a 2.6-fold increase over HTPB. Such a result is consistent with the low viscosity of the macro-crystalline wax (0.002 $\mathrm{Pa \cdot s}$ at 423 K, see Section 5.1), that promotes entrainment mass transfer. The viscosity of J1 is nearly 66% lower than that of the micro-crystalline wax used in Refs. [11,14]. This contributes to the faster $\dot{r}_f$, although a direct comparison is hindered by the different data reduction methods. The armored grains exhibit slightly augmented $\dot{r}_f$ with respect to the baseline. This result suggests that the entrainment phenomenon is not hampered by the presence of the structure: apparently, the addition of the 3D-printed scaffold does not alter melt layer viscosity. The reinforcing structure and the paraffin matrix show different $\dot{r}_f$, since PLA exhibits pyrolyzing combustion, while the J1 burns by vaporization and shows entrainment mass transfer. Under the investigated conditions, the data scattering in Table 9 limits considerations about the most performing reinforcement topology, when considering the $\dot{r}_f$ as a metric. Yet, the SP-based armored grain shows attractive $\dot{r}_f$ enhancements over the baseline: 36% for $\overline{G}_{ox}$ of $\sim$ 40 $\mathrm{kg/(m^2 \cdot s)}$. The enhanced ballistic performance of armored grains is also captured by the fuel mass flow rate ($\Delta m_b / \Delta t_b$, see Table 9).

Tested specimens feature $\overline{G}_{ox}$ in the range 37 to 46 $\mathrm{kg/(m^2 \cdot s)}$ and average chamber pressure in the range 0.93 to 1.08 MPa. The relatively narrow range of the average oxidizer mass flux enables a comparison of the achieved $\dot{r}_f$. HTPB is the fuel showing the lowest combustion chamber pressure. Pressure values around 0.96 - 1.0 MPa are reached by armored grains, with the SH and TH formulations featuring the lowest values. Ballistic data show that, under the investigated conditions, SH does not significantly contribute to $\dot{r}_f$ enhancement, while TH provides performance similar to that of the GY. Such a difference between the honeycomb-based structures is possibly due to the swirl effect and the higher turbulence likely induced by the TH with respect to the SH. In this respect, GY surface is more irregular, providing similarities with the SH.

The fast burning behavior of the armored grains is likely due to the inner frame that, during the combustion, promotes turbulence, augments the heat feedback to the fuel surface and the mixing of reactants, and possibly affects local conditions for entrainment mass transfer. The embedded reinforcing structure could increase the surface skin friction coefficient. Convective heat transfer coefficient enhancement for uneven surfaces as the internal port of armored grains is well-established [52]. A $\dot{r}_f(\overline{G}_{ox})$ dependence in the case of uneven regression surface is discussed

Table 9
Results of the ballistic tests of armored grains and comparison with pure paraffin J1. Conventional HTPB is reported for completeness.

Specimen	Regression rate $\dot{r}_{f,MB}$ (mm/s)	Regression rate increment $\Delta\dot{r}_{f,MB}$ (%)	Fuel mass flow rate $\Delta m_b/\Delta t_b$ (g/s)	Oxidizer mass flux $\bar{G}_{ox}$ (kg/(m^2·s))
HTPB [51]	0.8 ± 0.1	-63	1.6 ± 0.2	37 ± 3
J1	2.3 ± 0.2	-	4.1 ± 0.3	40 ± 3
J1_GY_i15	2.8 ± 0.2	25	5.6 ± 0.3	37 ± 3
J1_SP_i15	3.1 ± 0.2	36	6.3 ± 0.4	39 ± 1
J1_SH_i15	2.6 ± 0.1	16	5.3 ± 0.6	41 ± 5
J1_TH_i15	2.9 ± 0.1	27	5.3 ± 0.3	46 ± 3

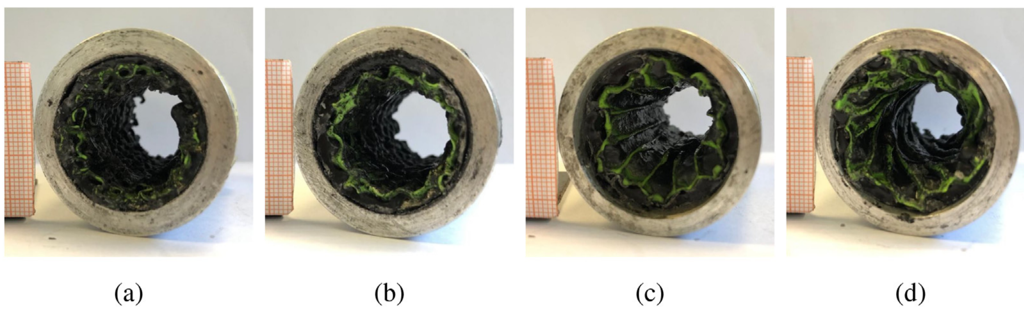

Fig. 16. Armored grains: head-ends after the firing tests of (a) J1_GY_i15, (b) J1_SP_i15, (c) J1_SH_i15, and (d) J1_TH_i15.

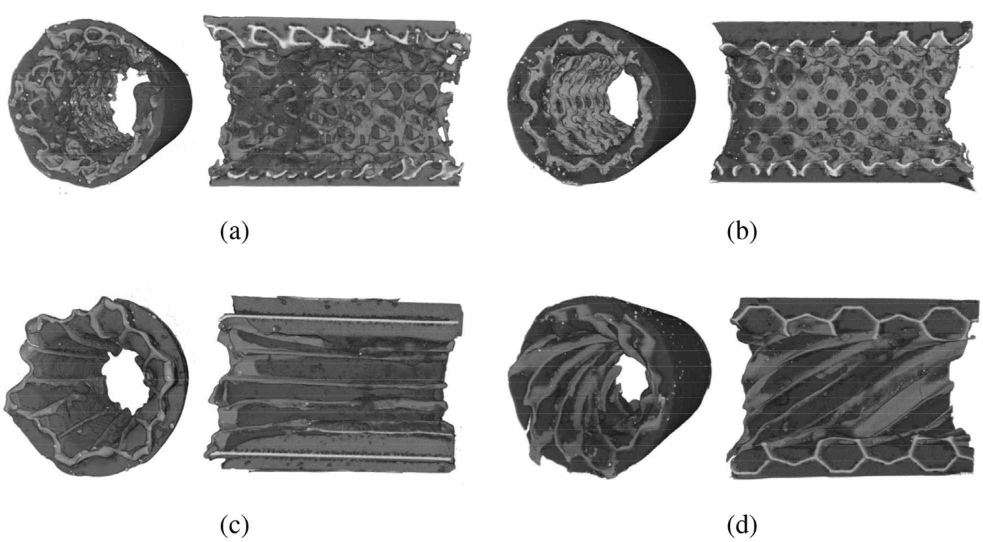

Fig. 17. X-ray tomographies of armored grains featuring different PLA reinforcements after the firing tests: head-end and cross-sectional views for (a) J1_GY_i15, (b) J1_SP_i15, (c) J1_SH_i15, and (d) J1_TH_i15. Note: the paraffin matrix is in dark gray/black, the PLA structure in light gray.

in Ref. [14]: surface irregularities yield the classical power-law dependence from an exponent < 1, to 1. The J1 fuel and the armored grains after the firing are shown in Figs. 15 and 16, respectively. The different texture of the burning surfaces can be appreciated: a relative smoothness characterizes J1 (where only roll waves can be identified, see also [13]), while armored grains show an uneven and rough surface. Protrusions are expected to affect the fuel regression enhancement through: (i) boundary layer detachment and reattachment [53,54], (ii) surface roughness (both at local level due to the FDM-printed structure surface, and globally - because of the embedded structure), (iii) recirculation zones favoring fuel and oxidizer mixing efficiency [55]. The combination of these physical phenomena is expected to yield higher Nusselt and Stanton numbers, and, in turn, enhanced convective heat transfer [56]. The PLA shows a relatively low $\dot{r}_f$ with respect to the J1 (see results reported in Refs. [29,42]), and this yields the complex regressing surface morphology observed in Figs. 16 and 17. Based on the thermal properties determined by the DTA-TG analyses, together with the tomographies and images of post-fired grains (Figs. 16, 17), the embedded PLA reinforcement retains (at least partially) the cellular structure morphology. Although the regression surface of armored grains is characterized by irregularities, the central port shape remains quasi-circular (see Figs. 18-21). Turbulence enhancement is not expected to be the only effect of the armored grains: GY, SP, and TH could also retain paraffin during the firing possibly preventing fuel slumping. J1_SH_i15 likely represents an exception, since it shows only a limited increase in $\dot{r}_f$ and appears less effective in promoting turbulence, mixing, and paraffin retention. The SH shows only a limited increase in $\dot{r}_f$ with respect to the other reinforcements, and can retain paraffin only by the cell walls. This peculiarity may be linked to a globally smoother fuel surface with respect to the other configurations (see Fig. 17). Yet, investigated conditions do not allow a systematic evaluation of slump effects, nor of combustion efficiency. The latter parameter could benefit from the intricate structure of GY, SP, and TH, but detailed analyses are needed to clarify this possibility.

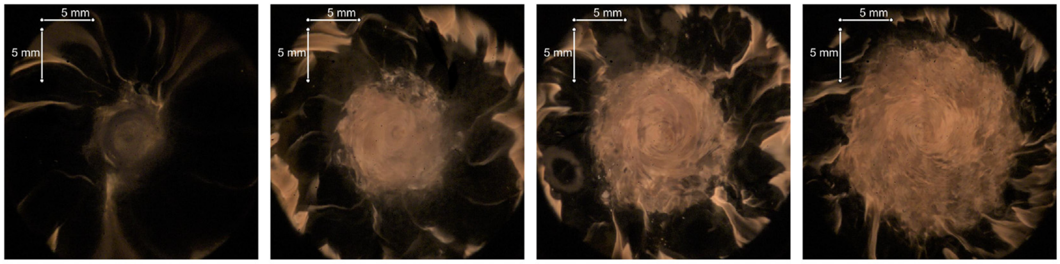

(a) (b) (c) (d)

Fig. 18. Combustion evolution of a gyroid-armored grain with an initial port diameter of 5 mm: (a) $t = t_0$, (b) $t = t_0 + 1$ s, (c) $t = t_0 + 2.25$ s, (d) $t = t_0 + 3.5$ s.

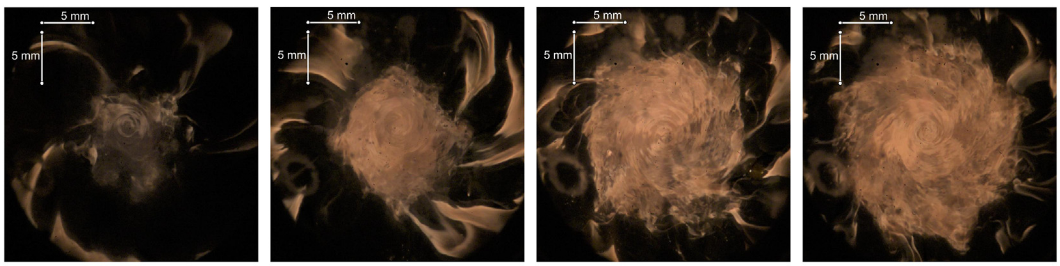

(a) (b) (c) (d)

Fig. 19. Combustion evolution of a Schwarz-P-armored grain with an initial port diameter of 5 mm: (a) $t = t_0$, (b) $t = t_0 + 1$ s, (c) $t = t_0 + 2.25$ s, (d) $t = t_0 + 3.5$ s.

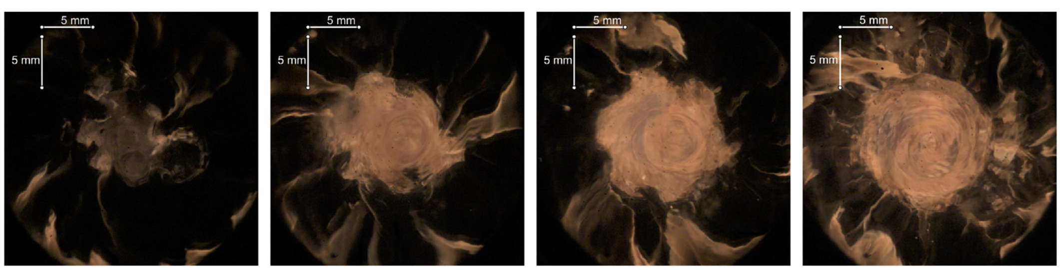

(a) (b) (c) (d)

Fig. 20. Combustion evolution of a honeycomb-armored grain with an initial port diameter of 5 mm: (a) $t = t_0$, (b) $t = t_0 + 1$ s, (c) $t = t_0 + 2.25$ s, (d) $t = t_0 + 3.5$ s.

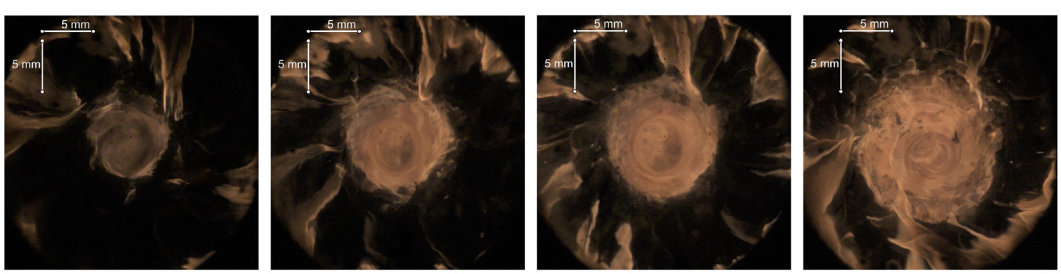

(a) (b) (c) (d)

Fig. 21. Combustion evolution of a twisted honeycomb-armored grain with an initial port diameter of 5 mm: (a) $t = t_0$, (b) $t = t_0 + 1$ s, (c) $t = t_0 + 2.25$ s, (d) $t = t_0 + 3.5$ s.

6. Conclusion and future developments

In this paper, the impact of 3D-printing on the structural and ballistic performance of paraffin-based fuels was studied. PLA and a macro-crystalline paraffin wax were employed for the 3D-printed structures and the paraffin fuel matrix, respectively. The reinforced formulations were named *armored grains*. The selected geometries for the reinforcements were the gyroid (GY), the Schwarz-P (SP), the straight honeycomb (SH), and the twisted honeycomb with a 1/4 turn per inch (TH). The armored grains consisted of a 7% to 15% volume fraction (or relative density) of polymeric reinforcement embedded in a macro-crystalline wax.

The structural assessment of the selected reinforcing structures was verified via compression tests and supported by finite element analysis. A sudden stress drop beyond the ultimate compressive strength was observed for the honeycombs, whereas the GY and the SP responded to compression by a constant and homogeneous crumpling. This demonstrated the different collapsing mechanism of the structures (stretch-dominated for the honeycombs, bending-dominated for the GY and SP). The honeycomb-like structures (SH and TH) showed increased yield stress values with respect to the GY and the SP. Considering the gyroids, the results highlighted the correlation between higher volume fractions and higher mechanical properties. Although the FEA results overestimated the actual structural behavior, the numerical simulations confirmed the experimental findings. The numerical and experimental results of honeycombs are in good agreement, suggesting that the 3D-printing process introduces fewer defects in the printed honeycombs with respect to the other structures.

The assessment of the armored grains involved mechanical tests at compression and a ballistic test campaign. The insertion of 3D-printed structures turned the brittle behavior of the pure paraffin into a ductile one. The yield stress was increased by 10% to ∼340%, with the SP and the SH providing the lowest and the highest improvement, respectively. Considering the investigated GY-armored grains, the mechanical enhancement was strictly related to the increment of the volume fraction of the embedded structure. The stress-strain trends of the armored grains followed the ones of the reinforcing structures: the honeycomb-armored grains featured a sudden drop of their mechanical properties after the yield point, whereas the GY- and the SP-armored grains exhibited a plateau stress after the yield point. The feasibility of exploiting FEA to predict the mechanical behavior of armored grains was assessed considering the smallest repetitive unit, i.e. the *armored cube*. Future research activity will extend the numerical studies to model the entire armored grains. From the ballistic point of view, the regression rate of paraffin-based formulations was increased by 15% to 35% when embedding the cellular structures in the fuel grain. The firing tests showed that the armored grains burn even faster than the pure paraffin fuels, despite the fact that the PLA employed for the reinforcement is a slow-burning material. This evidences that the entrainment phenomenon was not suppressed by the embedded structure. The augmented ballistic response was probably achieved thanks to the uneven and rough burning surface produced by the inner polymeric structure. This enhanced the heat transfer mechanism (increased friction, and oxidizer/fuel mixing). In the research, improved mechanical properties with respect to the pristine paraffin grains were observed for the armored grains, without lowering the regression rate performance of the wax fuel. Among the investigated armored grains, the gyroid shows an appealing compromise between mechanical and ballistic performance enhancements, as highlighted also by the FEA analyses. The GY exhibits high yield stress, plastic behavior, and a fast regression rate.

The armored grain proved to be a promising solution for the development of high-performance hybrid rockets featuring excellent mechanical and ballistic characteristics. The results of the present work and the previous studies carried out at the SPLab of Politecnico di Milano make the armored grain a suitable answer for the long-standing research for green paraffin-based fuels featuring both structural and combustion performance. Still, the feasibility of the armored grain concept for real flying systems has to be addressed by larger-scale tests. Future developments of the work will focus on finite element analysis to investigate the entire armored grains under different load conditions, whereas burning analyses will be extended to a larger scale to inspect the feasibility of the armored grain concept for propulsive applications, this step should be combined with the evaluation of the combustion efficiency of armored grains with respect to the non-armored counterparts.

Funding

This research did not receive any specific grant from funding agencies in the public, commercial, or not-for-profit sector.

CRediT authorship contribution statement

Riccardo Bisin: Methodology, Investigation, Writing – original draft, Formal analysis, Data curation, Software. **Francesco Calabró:** Visualization, Formal analysis, Data curation. **Christian Paravan:** Conceptualization, Methodology, Formal analysis, Writing – review & editing, Supervision.

Declaration of competing interest

The authors declare that they have no known competing financial interests or personal relationships that could have appeared to influence the work reported in this paper.

Acknowledgement

The authors thank Mr. Simone Parolini for his help with experimental data collection and supportive attitude.

Tomographic images of the armored grains were obtained thanks to the collaboration of the Advanced Manufacturing Laboratory (AMALA) of Politecnico di Milano, and, in particular, of Prof. Filippo Maggi.

References

[1] A. Mazzetti, L. Merotto, G. Pinarello, Paraffin-based hybrid rocket engines applications: a review and a market perspective, Acta Astronaut. 126 (2016) 286–297, doi:10.1016/j.actaastro.2016.04.036.
[2] A. Okninski, On use of hybrid rocket propulsion for suborbital vehicles, Acta Astronaut. 145 (2018) 1–10, doi:10.1016/j.actaastro.2018.01.027.
[3] C. Schmierer, M. Kobald, K. Tomilin, U. Fischer, S. Schlechtriem, Low cost small-satellite access to space using hybrid rocket propulsion, Acta Astronaut. 159 (2019) 578–583, doi:10.1016/j.actaastro.2019.02.018.
[4] M.A. Karabeyoglu, D. Altman, B.J. Cantwell, Combustion of liquefying hybrid propellants: part 1, general theory, J. Propuls. Power 18 (3) (2002) 610–620, doi:10.2514/2.5975.
[5] M.A. Karabeyoglu, B.J. Cantwell, Combustion of liquefying hybrid propellants: part 2, stability of liquid films, J. Propuls. Power 18 (3) (2002) 621–630, doi:10.2514/2.5976.
[6] B. Cantwell, A. Karabeyoglu, D. Altman, Recent advances in hybrid propulsion, Int. J. Energ. Mater. Chem. Propuls. 9 (4) (2010) 305–326, doi:10.1615/IntJEnergeticMaterialsChemProp.v9.i4.20.
[7] HyImpulse, Hyimpulse technologies (website), https://www.hyimpulse.de/en/. Accessed: 2025-12-11.
[8] Gilmour Space Technologies, Gilmour space technologies (website), https://www.gspace.com/. Accessed: 2025-12-03.
[9] TiSpace, Tispace (website), https://tispace.com/en. Accessed: 2025-12-03.
[10] Innospace, Innospace (website), https://www.innospc.com/. Accessed: 2025-12-13.
[11] R. Bisin, C. Paravan, S. Alberti, L. Galfetti, A new strategy for the reinforcement of paraffin-based fuels based on cellular structures: the armored grain – mechanical characterization, Acta Astronaut. 176 (2020) 494–509, doi:10.1016/j.actaastro.2020.07.003.
[12] C. Paravan, L. Galfetti, F. Maggi, A critical analysis of paraffin-based fuel formulations for hybrid rocket propulsion, AIAA Paper 2017–4830, 2017, doi:10.2514/6.2017-4830.
[13] C. Paravan, L. Galfetti, R. Bisin, F. Piscaglia, Combustion processes in hybrid rockets, Int. J. Energ. Mater. Chem. Propuls. 18 (3) (2019) 255–286, doi:10.1615/intjenergeticmaterialschemprop.2019027834.
[14] R. Bisin, C. Paravan, A new strategy for the reinforcement of paraffin-based fuels based on cellular structures: the armored grain – ballistic characterization, Acta Astronaut. 206 (2023) 284–298, doi:10.1016/j.actaastro.2023.02.027. https://www.sciencedirect.com/science/article/pii/S0094576523000930
[15] C.S. Clair, D. Gramer, E. Rice, W. Knuth, Advanced cryogenic solid hybrid rocket engine developments - Concept and test results, 4th AIAA/ASME/SAE/ASEE Joint Propulsion Conference and Exhibit, 2012, doi:10.2514/6.1998-3508.
[16] H. Bennet, Industrial Waxes. Volume 1: Natural & Synthetic Waxes, Chemical Publishing Company, Inc., New York, 1975.
[17] H. Bennet, Industrial Waxes. Volume 2: Compounded Waxes & Technology, Chemical Publishing Company, Inc., New York, 1975.
[18] K. Veale, S. Adali, J. Pitot, M. Brooks, A review of the performance and structural considerations of paraffin wax hybrid rocket fuels with additives, Acta Astronaut. 141 (2017) 196–208, doi:10.1016/j.actaastro.2017.10.012.
[19] M. Kobald, C. Schmierer, H. Ciezki, S. Schlechtriem, E. Toson, L.T. De Luca, Viscosity and regression rate of liquefying hybrid rocket fuels, J. Propuls. Power 33 (5) (2017) 1245–1251, doi:10.2514/1.B36207.
[20] J.C. Thomas, C. Paravan, J.M. Stahl, A.J. Tykol, F.A. Rodriguez, L. Galfetti, E.L. Petersen, Experimental evaluation of HTPB/paraffin fuel blends for hybrid rocket applications, Combust. Flame 229 (2021) 111386, doi:10.1016/j.combustflame.2021.02.032.

[21] S. Kim, H. Moon, J. Kim, J. Cho, Evaluation of paraffin polyethylene blends as novel solid fuel for hybrid rockets, J. Propuls. Power 31 (6) (2015) 1750–1760, doi:10.2514/1.B35565.

[22] D. Mengu, R. Kumar, Development of EVA-SEBS based wax fuel for hybrid rocket applications, Acta Astronaut. 152 (2018) 325–334, doi:10.1016/j.actaastro.2018.08.034.

[23] K. Bilge, U. Kokal, N.B. Emerce, U.C. Yildiz, M. Baysal, A. Karabeyoglu, Selection criteria for tackifier addition to paraffin wax based hybrid rocket fuels, AIAA Paper 2019–3921, 2019, doi:10.2514/6.2019-3921.

[24] Y. Tang, S. Chen, W. Zhang, R. Shen, L.T. De Luca, Y. Ye, Mechanical modifications of paraffin-based fuels and the effects on combustion performance, Propellants Explos. Pyrotech. 42 (11) (2017) 1268–1277, doi:10.1002/prep.201700136.

[25] S.A. Whitmore, Z.W. Peterson, S.D. Eilers, Comparing hydroxyl terminated polybutadiene and acrylonitrile butadiene styrene as hybrid rocket fuels, J. Propuls. Power 29 (3) (2013) 582–592, doi:10.2514/1.B34382.

[26] S.A. Whitmore, S.D. Walker, D.P. Merkley, M. Sobbi, High regression rate hybrid rocket fuel grains with helical port structures, J. Propuls. Power 31 (6) (2015) 1727–1738, doi:10.2514/1.B35615.

[27] S.A. Whitmore, S.L. Merkley, L. Tonc, S.D. Mathias, Survey of selected additively manufactured propellants for arc ignition of hybrid rockets, J. Propuls. Power 32 (6) (2016) 1494–1504, doi:10.2514/1.B36106.

[28] C. Oztan, V.L. Coverstone, Utilization of additive manufacturing in hybrid rocket technology: a review, Acta Astronaut. 180 (2021) 130–140, doi:10.1016/j.actaastro.2020.11.024. https://www.sciencedirect.com/science/article/pii/S0094576520307001

[29] C. Nguyen, J.C. Thomas, Performance of additively manufactured fuels for hybrid rockets, Aerospace 10 (6) (2023) 1–34, doi:10.3390/aerospace10060500. Paper no. 500, Published: 25 May 2023.

[30] J. McCulley, A. Bath, S.A. Whitmore, Design and testing of FDM manufactured paraffin-ABS hybrid rocket motors, AIAA Paper 2012–3962, 2012, doi:10.2514/6.2012-3962.

[31] J.E. Lyne, A. Brigham, R. Savery, K. Karcher, J. Pyron, L. Adams, G. Reagan, H. Furches, D. Sola, L. Melendez, The use of a 3-D printed, polymer matrix containing pulverized fuel in a hybrid rocket, AIAA Paper 2018–4597, 2018, doi:10.2514/6.2018-4597.

[32] D. Armold, J.E. Boyer, K. Kuo, J.K. Fuller, J. Desain, T.J. Curtiss, Test of hybrid rocket fuel grains with swirl patterns fabricated using rapid prototyping technology, AIAA Paper 2013–4141, 2013, doi:10.2514/6.2013-4141.

[33] D.M. Armold, J.E. Boyer, B. McKnight, K. Kuo, J. Desain, B.B. Brady, J. Fuller, T.J. Curtiss, Testing of hybrid rocket fuel grains at elevated temperatures with swirl patterns fabricated using rapid prototyping technology, AIAA Paper 2014–3754, 2014, doi:10.2514/6.2014-3754.

[34] G. Cai, Y. Zhang, Y. Zhang, J. Tian, H. Zhu, H. Tian, Research on the combustion and internal ballistic characteristics of paraffin-enhanced grains with dual-layer skeleton in hybrid rocket motors, Aerosp. Sci. Technol. 162 (2025) 110179, doi:10.1016/j.ast.2025.110179. https://www.sciencedirect.com/science/article/pii/S1270963825002500

[35] R. Bisin, C. Paravan, S. Alberti, L. Galfetti, An innovative strategy for paraffin-based fuels reinforcement: part I, mechanical and pre-burning characterization, in: 8th European Conference for Aeronautics and Space Sciences (EUCASS), Madrid, ES, 2019, pp. 1–14, doi:10.13009/EUCASS2019-718.

[36] R. Bisin, C. Paravan, A. Verga, L. Galfetti, An innovative strategy for paraffin-based fuels reinforcement: part II, ballistic characterization, in: 8th European Conference for Aeronautics and Space Sciences (EUCASS), Madrid, ES, 2019, pp. 1–9, doi:10.13009/EUCASS2019-728.

[37] A.H. Schoen, Infinite periodic minimal surface without self-intersections, NASA TN D–5541 (1970).

[38] C. Hill, C.C. McDougall, T. Messinger, C.T. Johansen, Modification of paraffin-based hybrid rocket fuels using structural lattices, AIAA Paper 2019–4191, 2019, doi:10.2514/6.2019-4191.

[39] D. Zdybal, W. Klos, P. Drozdz, Z. Rydz, K. Kobus, B. Wyciszkiewicz, A. Zwolak, M. Wyzlinski, T. Tatara, A. Guzik, Performance of solid state emulsions of isoamyl alcohol in EVA-stabilized, low-MW polyethylene, structured by laser-sintered nylon scaffolds as fuels N2O in hybrid rocket engine, AIAA Paper 2019–4335, 2019, doi:10.2514/6.2019-4335.

[40] J.A. Bresler, B. Natan, Experimental investigation of ABS-Paraffin 3D printed hybrid rocket fuels, AIAA Paper 2019–4094, 2019, doi:10.2514/6.2019-4094.

[41] C. Rontini, F. Giambelli, C. Paravan, Powder particle size and surface modification effects on aluminum-filled lattice structures in additive manufacturing of energetic materials, Powder Technol. 448 (2025) 120345, doi:10.1016/j.powtec.2025.120345.

[42] X. Yu, H. Yu, H. Gao, W. Zhang, L.T. DeLuca, R. Shen, 3D printed different polymer fuel grains for hybrid rocket engine, FirePhysChem 4 (2) (2024) 139–145, doi:10.1016/j.fpc.2023.10.001. Micromotors and Other Special Topics in Propulsion

[43] J.C. Dinis, T.F. Morais, P.H.J. Amorim, R.B. Ruben, H.A. Almeida, P.N. Inforçati, P.J. Bártolo, J.V.L. Silva, Open source software for the automatic design of scaffold structures for tissue engineering applications, Procedia Technol. 16 (2014) 1542–1547, doi:10.1016/j.protcy.2014.10.176.

[44] Y.-P. Wu, J.-F. Jiao, X.-G. Su, J.-T. He, J. Wang, Y.-J. Gong, W. Zhang, Z.-L. Qin, Combustion characteristics of vat-photopolymerized fuels with a spiral star port for hybrid propulsion, Langmuir 40 (21) (2024) 11155–11166, doi:10.1021/acs.langmuir.4c00864.

[45] ISO 604:2002, plastics – determination of compressive properties, International Organization for Standardization, 2002.

[46] Siemens Digital Industries Software, Femap website, 2025, https://www.plm.automation.siemens.com/global/it/products/simcenter/femap.html. Accessed: 2025-11.

[47] Siemens Documentation, Element library reference, https://docs.plm.automation.siemens.com/data_services/resources/nxnastran/10/help/en_US/tdocExt/pdf/element.pdf. Accessed: 2025-11.

[48] WeWantToLearn, Wewanttolearn website, triply periodic minimal surfaces, 2019, https://wewanttolearn.wordpress.com/2019/02/03/triply-periodic-minimal-surfaces/. Accessed: 2025-05.

[49] Siemens Documentation, Basic nonlinear analysis user's guide, https://docs.plm.automation.siemens.com/data_services/resources/nxnastran/11/help/tdoc/en_US/pdf/bas_nonlinear.pdf. Accessed: 2025-11.

[50] M.F. Ashby, The properties of foams and lattices, Philos. Trans. R. Soc. A 364 (1838) (2006) 15–30, doi:10.1098/rsta.2005.1678.

[51] R. Bisin, S. Alberti, A. Verga, C. Paravan, L. Galfetti, Green fuels for rocket propulsion: current status and future perspectives of paraffin-based formulations, in: 70th International Astronautical Congress (IAC), Washington, DC, 2019, pp. 1–11.

[52] T.L. Bergman, A.S. Lavine, F.P. Incropera, D.P. DeWitt, Fundamentals of Heat and Mass Transfer, John Wiley & Sons Inc, 2017.

[53] R. Mittal, U. Madanan, R.J. Goldstein, The heat/mass transfer analogy for a backward facing step, Int. J. Heat Mass Transf. 113 (2017) 411–422.

[54] M. Sachdeva, R.J. Goldstein, V. Srinivasan, Local heat/mass transfer distributions on the bottom surface of a cavity exposed to an approaching turbulent boundary layer: aspect ratio effects, Int. J. Heat Mass Transf. 191 (2022) 122826.

[55] A. Basavaraju, J.C.H. Wong, C.T. Johansen, Regression rates of protrusion and lattice augmented fuel grains in hybrid rockets, J. Propuls. Power 41 (6) (2025) 754–763, doi:10.2514/1.B39865.

[56] R. Karwa, S.C. Solanki, J.S. Saini, Heat transfer coefficient and friction factor correlations for the transitional flow regime in rib-roughened rectangular ducts, Int. J. Heat Mass Transf. 42 (9) (1999) 1597–1615.